Journal of Turbulence
Volume 7, No. 71, 2006

Taylor & Francis
Taylor & Francis Group

Surface tension in incompressible Rayleigh–Taylor mixing flow

Y.-N. YOUNG*† and F. E. HAM‡

†Department of Mathematical Sciences, New Jersey Institute of Technology, Newark, NJ 07102, USA
‡Department of Mechanical Engineering, Stanford University, Stanford, CA 94305, USA

We study the effect of surface tension on the incompressible Rayleigh–Taylor instability. We modify Goncharov's local analysis [1] to consider the surface tension effect on the Rayleigh–Taylor bubble velocity. The surface tension damps the linear instability and reduces the nonlinear terminal bubble velocity. We summarize the development of a finite-volume, particle-level-set, two-phase flow solver with an adaptive Cartesian mesh, and results from convergence and validation studies of this two-phase flow solver are provided. We use this code to simulate the single-mode, viscous Rayleigh–Taylor instability with surface tension, and good agreement in terminal bubble velocity is found when compared with analytic results. We also simulate the immiscible Rayleigh–Taylor instability with random initial perturbations. The ensuing mixing flow is characterized by the effective mixing rate and the flow anisotropy. Surface tension tends to reduce the effective mixing rate and homogenizes the Rayleigh–Taylor mixing flow. Finally, we provide a scaling argument for detecting the onset of the quadratic, self-similar Rayleigh–Taylor growth.

Keywords: Rayleigh–Taylor instability; Surface tension; Anisotropy; Transition; Self-similar turbulence

PACS numbers: 52.35.Py; 47.11.Df; 68.03.−g; 68.03.Cd; 47.52.+j; 47.11.−j; 47.35.−i; 47.27.−i; 47.51.+a; 47.27.wj

1. Introduction

The Rayleigh–Taylor (RT) instability is a fingering instability of fluid interface when light fluid is accelerated against the heavy fluid. A principle focus of study on the Rayleigh–Taylor instability is the global mixing rate as the instability evolves and develops into turbulence. Recent simulations on miscible Rayleigh–Taylor instability show that the RT mixing rate depends sensitively on initial conditions [2–4]. Many other factors may influence the RT mixing, such as (numerical) mass diffusion [5, 6], surface tension [7], viscosity, compressibility [8], time dependence of driving acceleration, shocks, geometric effects and varied forms of heterogeneity.

Significant progress has accumulated from experiments, direct numerical simulations and analysis on the miscible RT mixing in the Boussinesq limit, where the density contrast is almost zero (the Atwood number $\mathcal{A} \equiv \frac{\rho^h - \rho^l}{\rho^h + \rho^l} \to 0$) and the buoyancy $\mathcal{A}g$ is finite (g is the acceleration). Experiments and simulations show that mass diffusion can reduce the RT mixing rate by as much as a half [9–12]. Analysis on the Boussinesq RT turbulence illustrates that the self-similar RT turbulence can be completely determined by the conditions at the onset of the

*Corresponding author. E-mail: yyoung@oak.njit.edu

Journal of Turbulence
ISSN: 1468-5248 (online only)
http://www.tandf.co.uk/journals
DOI: 10.1080/14685240600809979

self-similar process [13], where the mixing zone width (or amplitude) h grows quadratically with time ($h = \alpha g \mathcal{A} t^2$). This finding is consistent with the sensitive dependence of the mixing rate α on initial perturbations [2, 4, 14], as different initial conditions may lead to different flows at the onset of the self-similar RT growth. Once the self-similar growth is initiated, the energy containing scale increases ($l \sim \mathcal{A} g t^2$) whereas the Kolmogorov scale decreases with time ($\eta \sim (\mathcal{A}^2 g^2/\nu^3)^{-1/4} t^{-1/4}$). As time progresses, the inertial range becomes large enough for establishing the forward cascade in the energy spectrum, and turbulence will be fully developed in the RT mixing zone. For this miscible RT turbulence, the scaling and turbulent mixing are described by the phenomenological model [15]. Thus, from the initial growth of the instability to the asymptotic turbulent state, the evolution of Boussinesq miscible RT mixing can be completely characterized by the flow conditions at the transition to self-similar growth, which is estimated to occur at $t \sim 15 t_c = 15(\nu/g^2\mathcal{A}^2)^{1/3}$ [13]. It is unclear if the above Boussinesq results may be directly applied to the immiscible RT mixing with finite Atwood numbers.

Motivated by these studies on Boussinesq RT mixing, in this paper we focus on characterizing the immiscible RT instability by identifying the transition to the nonlinear evolution and the transition to the self-similar growth. In particular, we will focus on the effects of surface tension and finite Atwood number on transitions between different evolutionary stages.

For single-mode RT instability with $\mathcal{A} = 1$, the transition from linear to nonlinear dynamics occurs when the mode amplitude $h_k \sim 1/k$ [16], where k is the wavenumber. As the amplitude increases, the rising bubble will reach a constant terminal velocity. Goncharov [1] extended potential flow models in Layzer [17] and Hecht *et al*. [18] to an arbitrary Atwood number. He found the terminal bubble velocity v_b to be a function of $\mathcal{A}$:

$$v_b = \sqrt{\frac{2\mathcal{A}}{1+\mathcal{A}} \frac{g}{Ck}}, \tag{1}$$

where $C = 3$ (1) for two (three)-dimensional geometries. Recent results from simulations of single-mode RT instability show that Goncharov's model gives better agreement than other potential flow models (see [19] and references therein) and vortex sheet simulations by Sohn [20]. We will modify the local potential flow analysis in [1] to consider the surface tension effect on the single-mode Rayleigh–Taylor instability. Results from this analysis show that the terminal bubble velocity is reduced by surface tension. We will also compare the analytic prediction with direct simulation of single-mode, immiscible RT instability in section 3.

For a broadband of unstable modes, a quadratic, self-similar growth ensues after nonlinearity takes over the initial exponential growth of the RT instability. Dimonte [14] summarized how unstable modes grow and evolve to give rise to the self-similar RT turbulence. Assuming that each mode reaches a terminal velocity, independent of the other growing modes, the self-similar expansion is envisioned to be the result of a succession of dominant bubbles from small sizes at small amplitudes to large bubbles at large amplitudes. From this model, the self-similar quadratic growth is possible if the initial perturbation amplitudes vary inversely with the wavenumber $h_k \sim 1/k^2$. For the Boussinesq RT turbulence, a self-similar analysis [13] on the averaged moment equations shows that the mixing rate $\alpha = \frac{C_0}{4}(1 + \sqrt{\frac{4h_0}{\mathcal{A}gC_0t^2}})$, where C_0^2 is the variance of the density fluctuation at the center of the mixing zone. The self-similar solution requires C_0 to be a constant that is determined by the density variance at the onset of the self-similar turbulence. The onset of the self-similar growth is estimated to occur at $t = 15t_c$, when the diffusive regime ends. Such an estimate may not be reasonable for the immiscible RT instability, where there is no molecular mass diffusion. Refining the self-similar analysis in [13], we present a scaling argument that allows us to detect the onset of the self-similar growth without referring to the diffusion regime. With this we can estimate the transition to self-similar growth for immiscible RT mixing with large density contrast.

This paper is organized as follows. In section 2 we present the local potential flow analysis for single-mode RT instability. In section 3 we summarize the problem formulation of the viscous, immiscible RT instability and the numerics of the finite-volume, particle-level-set (FV-PLS) flow solver. We also provide detailed code validation and convergence results. In section 4 we present results of direct simulations of immiscible RT mixing for various values of surface tension and density contrast. Finally, in section 5 we propose a scaling argument for detecting the onset of the self-similar RT growth in general situations, and we also provide some future directions.

2. Surface tension effect on single-mode RT instability

In this section we consider the effect of surface tension on the RT instability of an inviscid ($\nu = 0$) potential flow. These analytic results will be used to validate the incompressible two-phase flow solver summarised in the next section.

In the analysis we assume the surface tension to be small enough for the instability to grow and form a bubble/spike configuration. The fluids are subject to an external acceleration g along the $\hat{y}$ axis, pushing the heavy fluid toward the light fluid. The fluid interface is located at $y = \eta(x, t)$, and the velocity potential ϕ obeys the Laplace equation

$$\nabla^2\phi = \left(\partial_x^2 + \partial_y^2\right)\phi = 0. \tag{2}$$

The governing equations for two irrotational, incompressible, inviscid fluids in two dimensions are

$$\partial_t\eta + u^h\partial_x\eta = v^h, \tag{3}$$

$$[v - u\partial_x\eta] = 0, \tag{4}$$

$$\left[\rho\left(\partial_t\phi + \frac{1}{2}\mathbf{u}^2 + g\eta\right)\right] + [P] = 0, \tag{5}$$

with velocity $\mathbf{u} = (u, v) = \nabla\phi$ and P is the pressure. $[Q] \equiv Q^h - Q^l$, where the superscripts h and l denote the heavy- and light-fluid variables, respectively. The pressure jump in equation (5) is equal to the surface tension force

$$[P] = P^h - P^l = -\sigma\kappa, \tag{6}$$

where σ is the surface tension coefficient and κ is the local curvature. We expand the bubble shape η in x near the bubble tip:

$$\eta = \eta_0(t) + \eta_2(t)x^2 + \mathcal{O}(x^3), \tag{7}$$

with $|x| \ll 1$ and η_2 is related to the bubble radius R as $R = -1/(2\eta_2)$. Following Goncharov's approach, we adopt the following velocity potentials at the bubble tip:

$$\phi^h = a_1(t)\cos(kx)\mathrm{e}^{-k(y-\eta_0)}, \tag{8}$$

$$\phi^l = b_1(t)\cos(kx)\mathrm{e}^{k(y-\eta_0)} + b_2(t)y, \tag{9}$$

where a_1, b_1 and b_2 are amplitudes to be determined. For the parabolic bubble profile in equation (7), the bubble curvature κ is approximated as

$$\kappa \sim \frac{-2\eta_2}{\sqrt[3]{1 + 4\eta_2^2x^2}} \sim -2\eta_2\left(1 - 6\eta_2^2x^2\right). \tag{10}$$

Substituting equations (8)–(9) into equation (5) and expanding in x around the bubble tip, we obtain the following equations at the zeroth order in x:

$$\dot{\eta}_2 = -\dot{\eta}_0 \tfrac{k}{2}(k + 6\eta_2), \tag{11}$$

$$\rho^h\left(\dot{a}_1 + \tfrac{1}{2}k^2a_1^2 + g\eta_0\right) - \rho^l\left(\dot{b}_1 + \dot{b}_2\eta_0 + \tfrac{1}{2}k^2b_1^2 + kb_1b_2 + \tfrac{1}{2}b_2^2 + g\eta_0\right) + 2\eta_2\sigma = 0. \tag{12}$$

a_1, b_1 and b_2 can be expressed in terms of η_0 and η_2 after we substitute ϕ^h and ϕ^l into equations (3)–(4):

$$\dot{a}_1 = -\frac{\ddot{\eta}_0}{k}, \quad b_1 = \frac{\dot{\eta}_0(k + 6\eta_2)}{k(k - 6\eta_2)}, \quad b_2 = \frac{12\dot{\eta}_0\eta_2}{6\eta_2 - k}. \tag{13}$$

Substituting the above expressions into equation (12) and linearizing with respect to the base state of a flat interface, we find the following linear equation for η_0:

$$\rho^h\left(-\frac{\ddot{\eta}_0}{k} + g\eta_0\right) - \rho^l\left(\frac{\ddot{\eta}_0}{k} + g\eta_0\right) - k^2\sigma\eta_0 = 0\ . \tag{14}$$

Assuming the form of normal mode for η_0 ($\eta_0 = \mathrm{e}^{nt}\eta_0'$), we find the linear growth rate

$$n = \sqrt{\mathcal{A}gk - \frac{k^3\sigma}{\rho^h + \rho^l}}, \tag{15}$$

which is identical to the linear analysis results for inviscid RT instability with surface tension [21]. At the quadratic order in x, the evolution equation for amplitude η_0 is obtained:

$$\ddot{\eta}_0\frac{k^2 - 4\mathcal{A}k\eta_2 - 12\mathcal{A}\eta_2^2}{2(k - 6\eta_2)} + \dot{\eta}_0^2k^2\frac{(4\mathcal{A} - 3)k^2 + 6(3\mathcal{A} - 5)k\eta_2 + 36\mathcal{A}\eta_2^2}{2(k - 6\eta_2)^2}$$
$$+ \mathcal{A}g\eta_2 - \frac{12\sigma\eta_2^3}{\rho^h + \rho^l} = 0. \tag{16}$$

Similar to Goncharov's analysis without surface tension, we find that, in the limit $t \to \infty$, the bubble curvature η_2 and the bubble velocity $\dot{\eta}_0$ approach their asymptotic values

$$\eta_2(t \to \infty) = -\frac{k}{6}, \quad \dot{\eta}_0(t \to \infty) = \sqrt{\frac{2\mathcal{A}}{1 + \mathcal{A}}\frac{g}{3k} - \frac{\sigma k}{9\rho^h}}. \tag{17}$$

For axi-symmetric RT bubbles, we obtain the following bubble curvature and terminal velocity:

$$\eta_2(t \to \infty) = -\frac{k}{8}, \quad \dot{\eta}_0(t \to \infty) = \sqrt{\frac{2\mathcal{A}}{1 + \mathcal{A}}\frac{g}{k} - \frac{3\sigma k}{16\rho^h}}. \tag{18}$$

It can be shown that the steady states in equations (17)–(18) are linearly stable to small perturbations.

In deriving equations (17)–(18) for the terminal bubble velocity, we have assumed a parabolic bubble shape with a curvature $-2\eta_2$. Therefore, the instability has to grow first for the analysis to be valid, and the condition

$$\sigma \le \sigma_c \equiv \frac{g(\rho^h - \rho^l)}{k^2} \tag{19}$$

must be satisfied for equations (17)–(18) and the above analysis with the surface tension to hold. From this condition, we obtain a lower bound on the bubble terminal velocity for a given

wavenumber and Atwood number

$$v_b > \sqrt{C \frac{2\mathcal{A}}{1+\mathcal{A}} \frac{g}{k}}, \tag{20}$$

where $C = \frac{2}{9}$ in two dimensions and $C = \frac{13}{16}$ in three dimensions.

In the next section we use results from the above analysis (equations (17)–(18)) to validate the FV-PLS two-phase flow solver. As will be illustrated, we obtain reasonable agreement between the analytic and the numerical results for small fluid viscosity ($\nu = 10^{-3}$) in the direct simulations of single-mode immiscible RT instability.

3. Formulation, numerics and validation

We first formulate the two-fluid system in the level-set framework. We then briefly summarize the essential numerics developed for the Cartesian adaptive grid. The key numerical development is the treatment of immersed, continuum surface tension force in the finite-volume fluid solver on the (homogeneously adaptive) Cartesian grid. We then present validation of using this two-phase solver to simulate the viscous, immiscible RT instability and mixing.

3.1 *Formulation and numerics*

The incompressible, immiscible, viscous two-fluid system is formulated as a one-fluid system with variations of density and viscosity only in the neighborhood of the interface. The fluid interface is described by a level-set function $\phi(\mathbf{x}, t) = 0$. With constant density and viscosity in each phase (fluid), the total density and viscosity can be written as

$$\rho = \rho(\phi) = \rho^h H(\phi) + \rho^l (1 - H(\phi)), \qquad \mu = \mu(\phi) = \mu^h H(\phi) + \mu^l (1 - H(\phi)), \tag{21}$$

where $\rho^{h,l}$ and $\mu^{h,l}$ are constant density and viscosity of the heavy or light fluid, respectively, and $H(\phi)$ is the Heaviside function: $H(\phi) = 1$ if $\phi > 0$ and $H(\phi) = 0$ if $\phi < 0$. Formulated as such, the continuity equation can be decomposed into the the following equations:

$$\frac{\partial \phi}{\partial t} + \mathbf{u} \cdot \nabla \phi = 0 \Big|_{\phi=0}, \quad \nabla \cdot \mathbf{u} = 0, \tag{22}$$

where $\mathbf{u}$ is the fluid velocity. Our numerical flow solver deals with the collocated velocities as the primitive variables; thus, the Navier–Stokes equations take the following form:

$$\rho \frac{\partial \mathbf{u}}{\partial t} + \rho \nabla(\mathbf{u}\mathbf{u}) = -\nabla p + \nabla(\mu \nabla \mathbf{u}) - \rho g \hat{k} + \sigma \kappa \delta(d) \hat{n}, \tag{23}$$

where p is the pressure, g is the gravitational acceleration, σ is the surface tension coefficient, κ is the local surface curvature, $\delta(d)$ is the delta function based on the normal distance d to the surface and $\hat{n}$ is the outward unit normal vector at the free surface. Equations (21)–(23) comprise the governing equations for the two-fluid system. It is important that we choose an accurate and efficient numerical scheme for evolving the level set to mitigate the numerical error in conserving mass and momentum. We solve equations (22)–(23) on a Cartesian adaptive grid. The grid arrangement and adaptation are described in [22], and here we only discuss details pertaining to the simulation of the two-phase flow.

All variables are stored at the control volume (CV) centers (with the exception of a face-normal velocity located at the face centers) and are used to enforce the divergence-free constraint at each time step. The variables are staggered in time for convenience in the time

advancement scheme; the velocities are located at time levels t^n and t^{n+1}; and pressure, density, viscosity and the level set at time levels $t^{n-1/2}$ and $t^{n+1/2}$. The semi-discretization of the governing equations at each time step is then as follows.

Step 1. Advance and reinitialize the level set

$$\frac{\phi^{n+1/2} - \phi^{n-1/2}}{\Delta t} + u_j^n \frac{1}{2} \frac{\partial}{\partial x_j}(\phi^{n-1/2} + \phi^{n+1/2}) = 0. \tag{24}$$

The spatial derivatives in the level-set equation (equation (24)) are approximated by a fifth-order WENO scheme [23]. Uniform, homogeneous grid refinement is enforced within a band around the zero level-set. For updating the level-set function, we use an implicit Crank–Nicholson scheme which requires an iterative method. In practice, the hyperbolic system is not stiff and can be quickly converged by a simple iterative scheme such as the Gauss–Seidel iteration. We note that in the present time-staggering scheme, equation (24) is decoupled from other equations and is advanced based on $\mathbf{u}^n$ to the next time level. The following reinitialization step is performed every step to ensure that the level set is a signed distance function

$$\frac{\partial \phi}{\partial \tau} = \mathrm{sgn}(\phi)(1 - |\nabla \phi|). \tag{25}$$

The spatial derivatives in reinitialization are once again approximated using the fifth-order WENO scheme. We use an explicit third-order TVD Runge–Kutta method for time integration. In practice, five iterations with a pseudo-time step of $\Delta\tau = \Delta x/4$ are sufficient.

In addition, we have utilized particles to improve the level set. Markers help minimize the movement of the level set during the reinitialization step, and reduce unnecessary merging of the level set due to numerical discretization/diffusion. This formulation is based on the hybrid-particle-level-set method [24]. Recent results show that the particle-level-set method is accurate and comparable to the most accurate front-tracking schemes. In standard tests such as the Zalesek disk and the time-reversal vortex flow, the particle-level-set method outperforms the usual level-set methods by reducing numerical diffusion [24, 25] in the level-set framework.

Step 2. Update the density and viscosity at $t^{n+1/2}$. With the level set advanced, fluid properties are calculated based on the level set at the mid-point of the time interval:

$$\begin{aligned} \rho^{n+1/2} &= \rho^h H(\phi^{n+1/2}) + \rho^l (1 - H(\phi^{n+1/2})), \\ \mu^{n+1/2} &= \mu^h H(\phi^{n+1/2}) + \mu^l (1 - H(\phi^{n+1/2})). \end{aligned} \tag{26}$$

In the present investigation, we use a smoothed property variation in the region of the zero level set as described by Sussman *et al*. [26]. This smoothed variation leads to a surface tension force that is of the C^2 class in the categorization for the immersed (continuous) delta function [27].

Step 3. Update the incompressible velocities at t^{n+1}. The procedures used to update the incompressible velocities are a variant of the collocated fractional step method [28]. We pay special attention to the discrete form of force terms that have rapid spatial variation around the interface, such as the surface tension forces in the momentum equation. First, a projected velocity field $\hat{u}_i$ is calculated:

$$\frac{\hat{u}_i - u_i^n}{\Delta t} = -\frac{1}{\rho^{n+1/2}} \left(\frac{\partial p}{\partial x_i}^{n-1/2} + R_i^{n+1/2} \right), \tag{27}$$

where R_i contains all other terms in the momentum equation. We discretize both the convective and viscous terms implicitly using second-order symmetric discretizations. The surface tension

is treated explicitly based on $\phi^{n+1/2}$ (the level set at the midpoint of the current time step). We then subtract the old pressure gradient and interpolate the velocity field to the faces. In the interpolation step, a critical difference between our formulation and the formulation of Kim and Choi [28] is in the calculation of the face-normal velocities. Kim and Choi assume

$$\overline{\frac{R_i^{n+1/2}}{\rho^{n+1/2}}}^{f} \approx \frac{R_f^{n+1/2}}{\rho_f^{n+1/2}}, \tag{28}$$

where $\overline{()}^{f}$ is a second-order interpolation operator that yields a face-normal component from two CV-centered vectors. This is an $O(\Delta x^2)$ approximation, seemingly consistent with the overall accuracy of the method, and significantly simplifies the calculation of the Poisson equation source term. However, when surface tension forces are introduced we find that this approximation can lead to large non-physical oscillations in the CV-centered velocity field. To solve this problem, the surface tension forces must be calculated at the faces and then averaged to the CV centers, i.e.

$$\frac{R_i^{\sigma}}{\rho} \equiv \overline{\frac{R_f^{\sigma}}{\rho_f}}^{x_i}. \tag{29}$$

With this calculation of the surface tension force, we have to include the additional terms in the calculation of the source term in the Poisson equation for the pressure.

3.2 *Code validation*

First, we illustrate the importance of a proper handling of the surface tension force. Figure 1(a) compares the calculated pressure along the horizontal center line: the dashed line is from using Kim and Choi's formulation for the surface tension force, and the solid line is from using equation (29). Clearly, our formulation results in a better pressure with a small amplitude of the velocity field (figure 1(b)) that should be exactly zero. These 'parasitic currents' have been reported by other investigators ([29], for example), and in our formulation the maximum parasitic velocity is on the order of $0.001\sigma/\mu$ for an equivalent uniform grid spacing $\Delta x = \frac{1}{64}$ and the Ohnesorge number $Oh \equiv (\mu^2/a\rho\sigma)^{0.5} = 2.1$. This is consistent with the observations of others using staggered structured codes. Figure 1(c) shows a comparison between the linear analysis results and the computed periodicity of capillary wave on a spherical drop, with generally good agreement, and the error in the capillary frequency is less than 1%.

Next, we present validation of using the FV-PLS two-phase flow solver to simulate the Rayleigh–Taylor instability. For these convergence tests, the computation domain size is $1 \times 1 \times 8$, and the originally flat interface is placed at $z = 4$. Periodic boundary conditions are adopted in the horizontal directions, and wall boundary conditions are used in the gravitational direction. We perturb the interface with a sinusoidal perturbation $a_0(\cos(kx) + \cos(ky))$, where the wavenumber $k = 2\pi$ and the amplitude $a_0 = 0.01$. The grid spacing for the velocity away from the interface is fixed at $\Delta x_f = 0.2$, and we vary the minimum grid spacing around the interface Δx_s from 0.2 to 0.025.

The results in figure 2(a) are for the Atwood number $\mathcal{A} = 0.1$ and the kinetic viscosity $\nu^h = \nu^l = 10^{-3}$. As shown in figure 2(a), the bubble height (h_b) converges as we decrease Δx_s. Similar convergence is also found for the down-welling spikes in these $\mathcal{A} = 0.1$ simulations. For the Atwood number $\mathcal{A} \sim 1$, the spikes of the heavy fluid are (almost) free-falling into the light fluid [30], whereas the bubbles of the light fluid reach a terminal velocity [1]. Due to such asymmetry between bubble and spike, more resolution is necessary to resolve the pointy

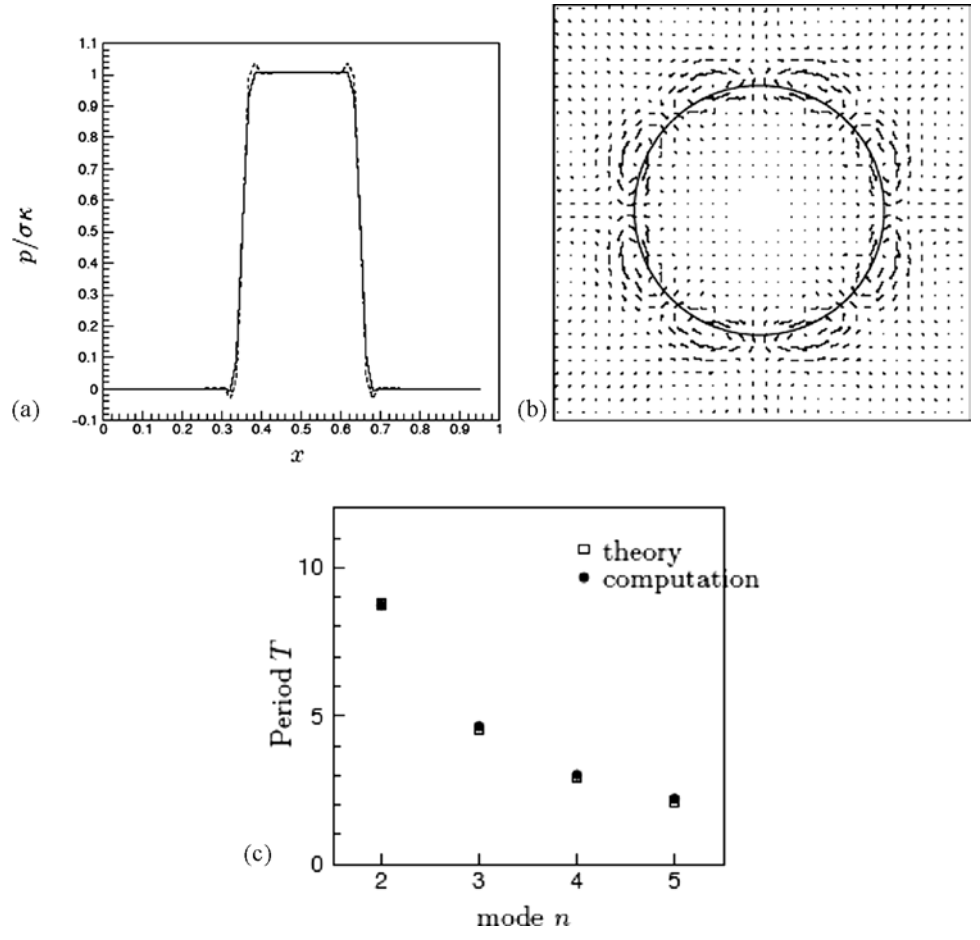

Figure 1. (a) A comparison of pressure for two different formulations of the surface tension force. The dashed line is from Kim and Choi's formulation and the solid line is from our formulation of the surface tension force. (b) Parasitic currents around a circular drop. The amplitude of the parasitic flow is $\sim 0.001\sigma/\mu$. (c) A comparison between computed and theoretical oscillation periods for a spherical drop.

spikes at large $\mathcal{A}$. Figure 2(b) shows the convergence of spike depth h_s as we decrease Δx_s from 0.2 to 0.0125. In figure 2(c) we show the order of convergence for results in panels (a) and (b). The second-order convergence for spikes with $\mathcal{A} = 0.9$ (solid line) is due to the fact that the error in the velocity field around the spike dominates the error in capturing the interface; thus, the order of convergence is that of the flow solver, which is of the second order [22]. However, for bubbles with $\mathcal{A} = 0.1$ (dashed line) the numerical error is dominated by that in capturing the interface; thus it is slightly larger than order 1.

Figure 3(a) demonstrates that, for a single-mode perturbation with $k = 2\pi$, $\sigma = 0$ and fluid viscosity $\nu^h = \nu^l = 10^{-3}$, the code reproduces the growth rate from linear analysis for Atwood numbers from 0.1 to 0.9 [21]. The sinusoidal perturbation grows exponentially and eventually saturates. During the nonlinear evolution, the bubble reaches a terminal velocity as shown in figure 3(b), where we plot the bubble velocity (scaled by equation (1)) versus the bubble height h_b. In figure 3(c) we plot the terminal bubble velocity from our simulations using two minimum grid spacings Δx_f. The solid line is the terminal bubble velocity from equation

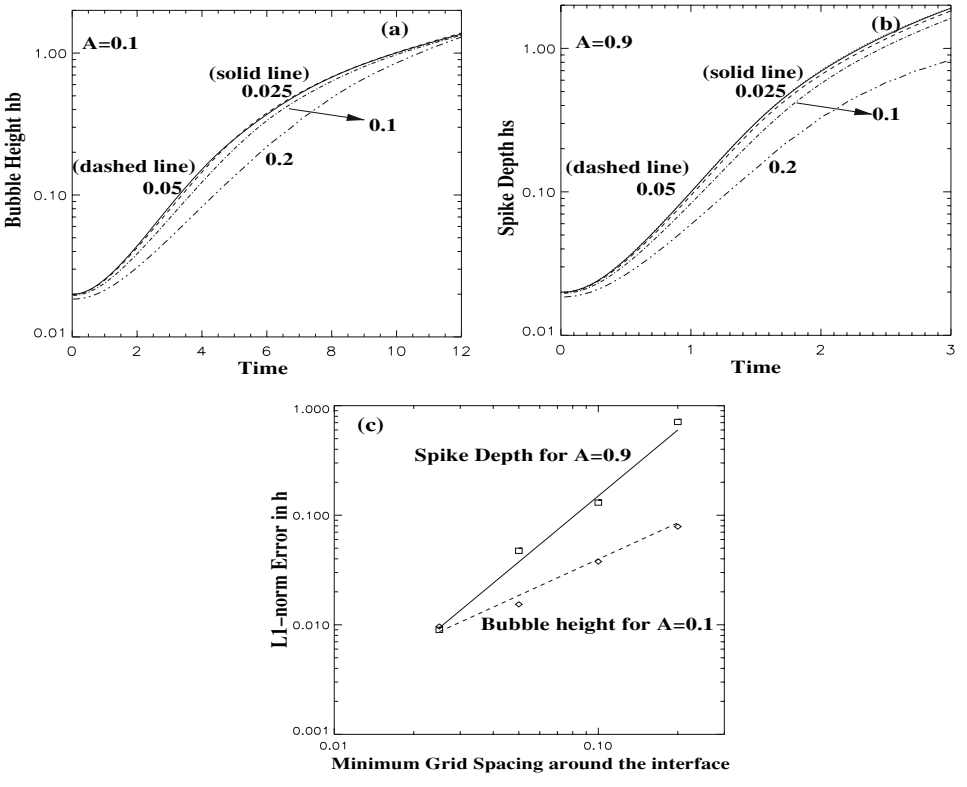

Figure 2. (a) Convergence test for bubble height for $\mathcal{A} = 0.1$. (b) Convergence test for spike depth for $\mathcal{A} = 0.9$. (c) L1-error versus Δx_s. The squares are for spike depth with $\mathcal{A} = 0.9$ and the diamonds are for bubble height with $\mathcal{A} = 0.1$. The solid line is proportional to $(\Delta x_s)^2$ and the dashed line is proportional to $(\Delta x_s)^{1.2}$.

(1). A comparison between numerical simulations of single-mode RT instability with several (inviscid) potential flow models shows that Goncharov's model gives the best agreement with simulation results for all values of the Atwood number [19]. In addition, the largest deviation between simulation results and Goncharov's model is found for the Atwood number $\mathcal{A} \sim 0.6$ [19], similar to our results in figure 3(c).

For small Atwood numbers in figure 3(b), the bubble velocity overshoots and decreases briefly before a second acceleration ensues. Similar late-time behavior is also found in two-dimensional RT single-mode. This second acceleration is first reported in [31]. Recently, Ramaprabhu and collaborators have reinvestigated this "second wind" in detail [32]. Their results show that the late-time acceleration is related to roll-up of vorticity around the bubble neck. The competition between form drag and skin friction governs the onset of the second acceleration. Thus, it is physically reasonable that the second acceleration may be delayed or even never occur for Atwood numbers close to unity. This conclusion is consistent with the trend we observe in figure 3(b).

We repeat simulations of the single-mode RT instability with surface tension coefficient $\sigma = 0.002$, $\Delta x_f = 0.05$ and $\Delta x_s = 0.0125$. Other parameters are the same as in previous simulations. Based on the convergence results in figure 2, we are confident that such spatial resolution is more than enough for numerically convergent simulations of the rising RT bubble with $\sigma = 0.002$. We simulate both two- and three-dimensional RT instability for two Atwood

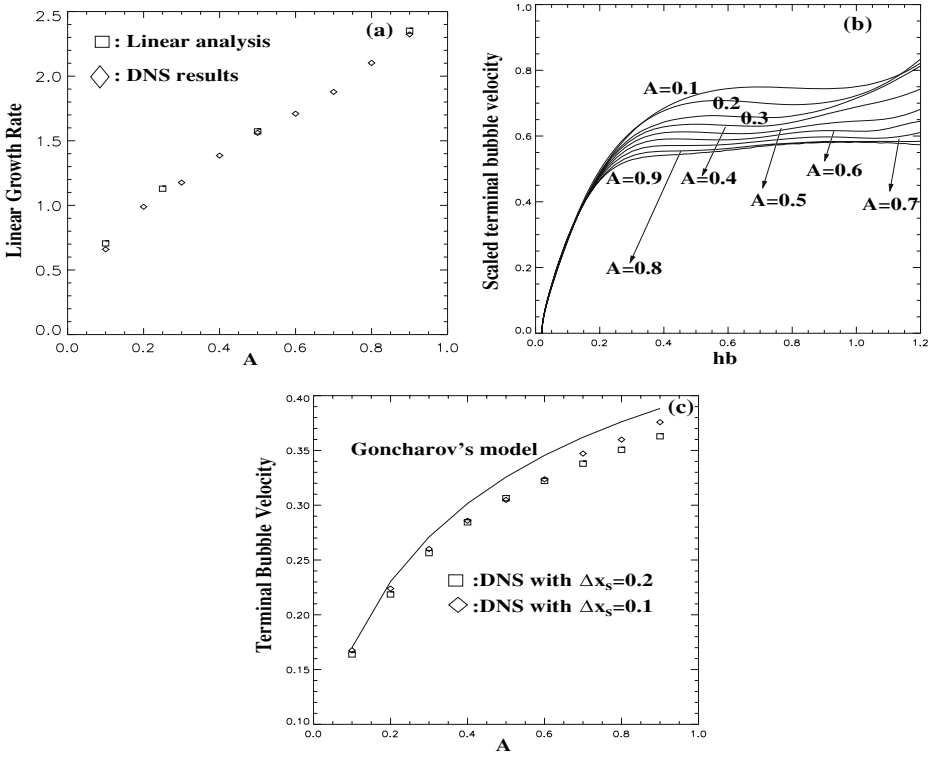

Figure 3. Code validation. (a) A comparison of the linear growth rate with analytic results. (b) Evolution of velocity of the Rayleigh–Taylor bubble from simulations. (c) A comparison of the terminal bubble velocity between simulations (symbols) and the nonlinear analysis (solid line).

numbers, $\mathcal{A} = 0.1$ and $\mathcal{A} = 0.99$. Figure 4 shows the evolution of the bubble velocity versus the bubble height. We scale the bubble velocity by the inviscid results in equations (17)–(18) with $\sigma = 0.002$. For $\mathcal{A} = 0.1$ the bubble velocity overshoots in both two- and three-dimensional cases, while for $\mathcal{A} = 0.99$ the bubble velocity uniformly approaches the analytical results.

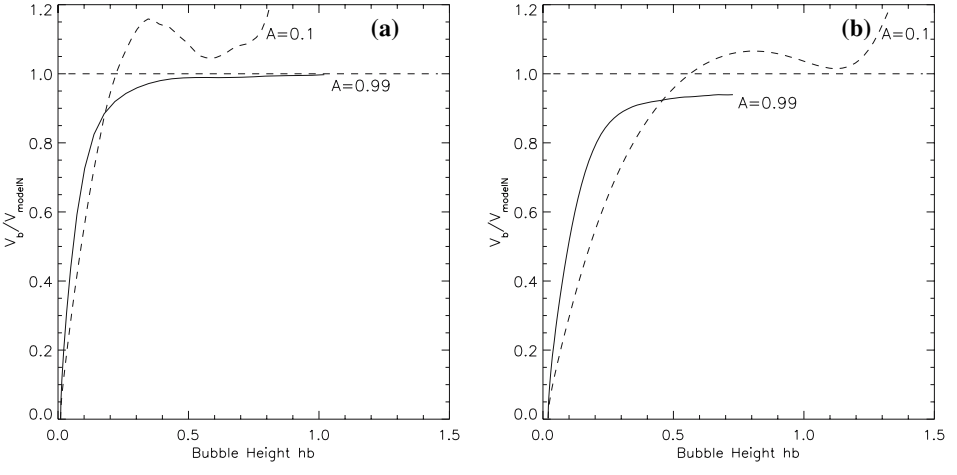

Figure 4. (a) Bubble velocity (scaled by equation (17)) for two-dimensional single-mode RT instability. (b) Bubble velocity (scaled by equation (18)) for three-dimensional single-mode RT instability.

4. Evolution of RT instability with random perturbation

Having validated the numerical code in both linear and weakly nonlinear regimes, in this section we focus on the consequence of perturbing the interface with a spatially random disturbance. For simulation results presented in the first half of this section (sections 4.1 and 4.2), the initial disturbance imposed at the interface is a white-noise random perturbation (with an amplitude 0.02). In section 4.1, we fix the Atwood number $\mathcal{A} = 0.3$ and vary the surface tension to investigate the effect of surface tension on RT mixing. We fix the surface tension coefficient $\sigma = 0.002$ and vary the Atwood number in section 4.2. In section 4.3 we focus on the evolution of turbulent RT mixing from random perturbations with smaller dominant wavelengths. We focus on how the RT mixing rate changes due to the surface tension. We also investigate how the surface tension force alters the anisotropy of the RT mixing flow.

In the numerical code, we adopt convenient non-dimensionalization so that the acceleration coefficient $g = 1$ and $\rho^h = 1$. Accordingly, the time is scaled by $T_0 = \sqrt{L/g}$ with L the horizontal domain size, and the dimensionless surface tension is $\sigma = \sigma_0/(g\rho L^2)$ where σ_0 is the dimensional surface tension coefficient and ρ is the dimensional density of the heavy fluid. Based on the characteristic bubble size λ and the density difference ($\Delta\rho$) between the two fluids, a similar non-dimensional surface tension coefficient can be defined as $\sigma' = \sigma_0/(g\Delta\rho\lambda^2)$ [7]. The relationship between the two dimensionless surface tension coefficients are

$$\sigma' = \sigma \frac{\rho}{\Delta\rho}\left(\frac{L}{\lambda}\right)^2. \tag{30}$$

In the following presentation and discussion, σ is used instead of σ' because as the random perturbation grows, the characteristic bubble diameter increases with time until it reaches the domain size L. Furthermore, from linear analysis, the initial characteristic bubble size depends on surface tension; the larger the surface tension, the larger the wavelength (λ) for the most unstable mode. As a result, σ is more convenient for quantifying the strength of the surface tension.

In all the following presentations, the time is reported in unit of $\sqrt{L/g}$, which is about 0.175 s for a container of horizontal size $L = 30$ cm and $g = 980$ cm s^{-2}.

4.1 $\mathcal{A} = 0.3$

For the following simulation results, the computation domain is $2 \times 2 \times 4$, viscosity $\nu = \frac{\mu}{\rho} = 10^{-3}$ for both fluids, $\Delta x_f = 0.05$ and $\Delta x_s = 0.0125$. Four values of the surface tension σ are used: $\sigma = 2 \times 10^{-6}$, 0.001, 0.002 and 0.004.

Figure 5 shows the evolution of the bubble amplitude h_b as a function of time for four different values of σ. The solid lines are from simulation data and the dashed lines are fits to the linear growth. For $\sigma = 2 \times 10^{-6}$ the linear growth starts after an initial transient, and the nonlinearity becomes "important"* at $t_{\rm nl} \sim 2.7$ when the bubble height $h_{\rm nl} \sim 0.10$. As the surface tension is small, we expect this case to be close to the miscible RT mixing with finite density contrast. For miscible, Boussinesq RT turbulence [13], the self-similar quadratic growth is estimated to start at $t = t_s \equiv 15t_c = 15(\nu/g^2\mathcal{A}^2)^{1/3}$, which is $t_s \sim 3.35$ in our time unit for $\mathcal{A} = 0.3$. Assuming that the self-similar growth also starts at t_s for miscible RT mixing with finite density contrast ($\mathcal{A} = 0.3$), our estimate for $t_{\rm nl} \sim 2.7$ is consistent with the estimated $t_s \sim 3.35$ because nonlinearity has to take over the linear regime before the self-similar growth. In section 5 we will discuss an alternative way to estimate the initiation of

* This is when the increase in bubble height deviates from the exponential growth by 5%.

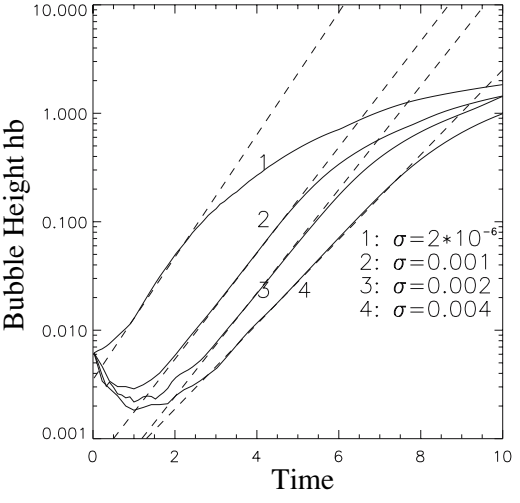

Figure 5. Bubble height versus time for four values of σ on a log-linear plot. $\mathcal{A} = 0.3$.

self-similar growth in immiscible RT mixing. We will also show that our estimate is in good agreement with the estimated $15t_c = 15(\nu/g^2\mathcal{A}^2)^{1/3}$ in [13].

As surface tension increases, the random perturbations decay first and undergo a long transient before they start to grow exponentially at a reduced growth rate (due to the surface tension, equation (15)). For large surface tension, nonlinearity becomes important later in time when the bubble amplitude is large. Therefore, both $h_{\rm nl}$ and $t_{\rm nl}$ increase with surface tension σ. These results are summarized in table 1. Also included in table 1 are the growth rate (slope of the dashed lines in figure 5), the wavenumber k_0 computed based on the growth rate n (measured from simulation data) and the inviscid dispersion relation (equation (15)), and the product $k_0 h_{\rm nl}$. Figure 6 illustrates the fluid interface at $t = t_{\rm nl}$ for both $\sigma = 2 \times 10^{-6}$ and $\sigma = 1 \times 10^{-3}$. From the peak in the spectrum of the fluid interface at $t_{\rm nl}$, we determine the dominant wavenumber k (in 2π). In this unit, the value listed in table 1 corresponds to the ratio L/λ in the computation domain.

Figure 7(a) shows the effective (or instantaneous) RT mixing rate $\alpha_{\rm eff} \equiv h/\mathcal{A}gt^2$ versus time. Figure 7(b) plots $\alpha_{\rm eff}$ versus the mixing zone width h. In table 1 we list the maximum effective mixing rate and the time when the maximum is reached. Also listed in table 1 is the duration $\Delta t = t_{\rm max} - t_{\rm nl}$. This duration appears to be independent of the surface tension σ. In all these simulations, the Reynolds number is $Re = \frac{\sqrt{ga^3}}{\mu/\rho} = 10^3$ in our non-dimensionalization. This value may be too low for the instability to reach the asymptotic limit where the mixing

Table 1. Summary for $\mathcal{A} = 0.3$ simulations. n is the growth rate (slope of the dashed lines in figure 5). Since $\nu = 10^{-3}$, we use equation (15) to approximate the most unstable wavenumber from the computed growth rate n and denote this approximation by k_0.

σ	k (2π)	n	k_0	$h_{\rm nl}$	$k_0 \times h_{\rm nl}$	$t_{\rm nl}$	max $(\alpha_{\rm eff})$	$t_{\rm max}$	h $(t_{\rm max})$	$\Delta t = t_{\rm max} - t_{\rm nl}$
2×10^{-6}	6	1.3	5.64	0.1	0.56	2.7	0.074	7.3	1.19	4.6
1×10^{-3}	4	1.13	4.5	0.15	0.68	5.0	0.057	9.8	1.65	4.8
2×10^{-3}	3	1.1	4.4	0.2	0.88	6.0	0.054	10.8	1.90	4.8
4×10^{-3}	1	0.9	2.9	0.3	0.87	7.5	0.042	12.2	1.81	4.7

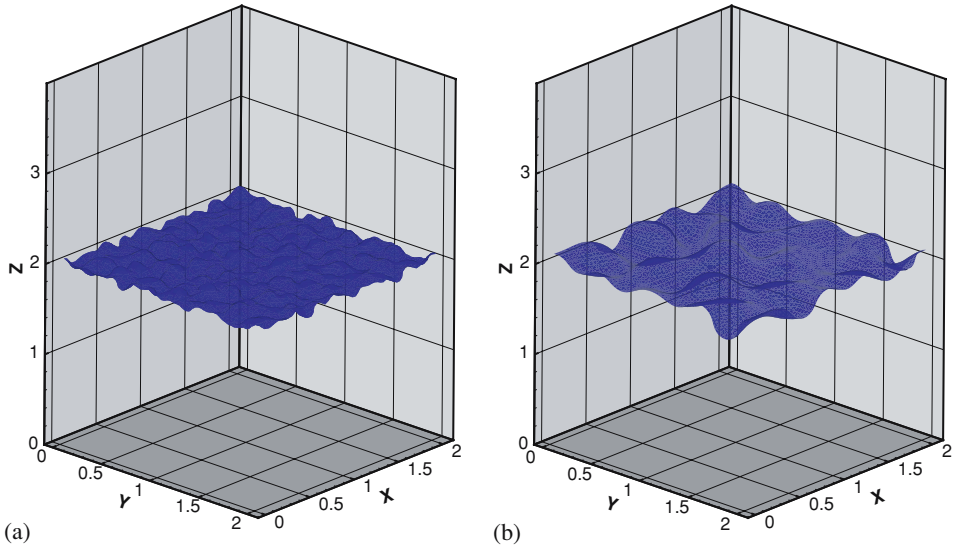

Figure 6. Fluid interface at the onset of nonlinear evolution $t = t_{\rm nl}$ for $\mathcal{A} = 0.3$ and (a) $\sigma = 2 \times 10^{-6}$, (b) $\sigma = 1 \times 10^{-3}$.

rate α stays constant in the RT turbulence. In addition, the finite computation domain also prevents α reaching the asymptotic value.

In the Boussinesq miscible RT mixing [11, 13], the dominant longitudinal (parallel to the acceleration) component contains more than 66% of the total kinetic energy throughout the evolution. A similar anisotropic partition of kinetic energy is found in the immiscible simulations, and figure 8 illustrates how such anisotropic partition of kinetic energy is affected by surface tension. These partitions of kinetic energy are related to the non-dimensional Reynolds stress anisotropy tensor [13]

$$b_{ij} = \frac{\langle u_i u_j \rangle}{\langle u_l u_l \rangle} - \frac{1}{3}\delta_{ij}, \tag{31}$$

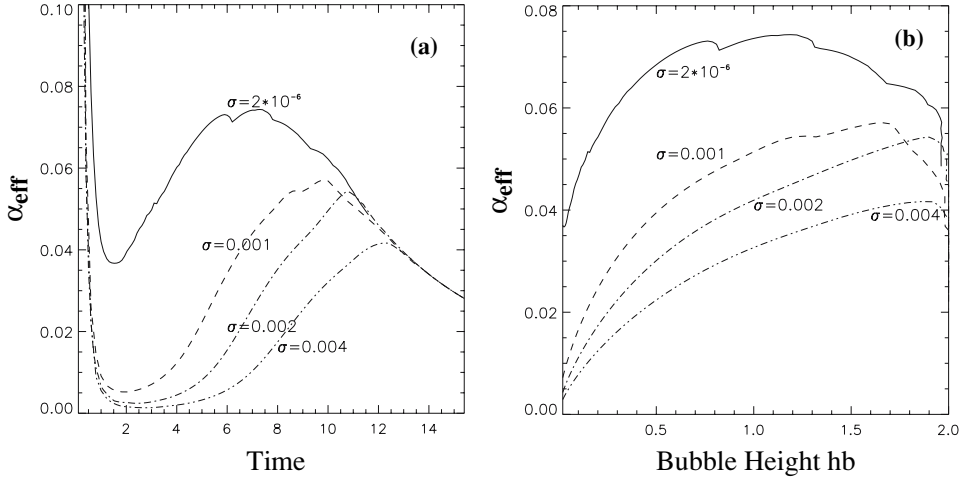

Figure 7. (a) Effective mixing rate $\alpha_{\rm eff} \equiv h/\mathcal{A}gt^2$ versus time. (b) $\alpha_{\rm eff}$ versus h_b.

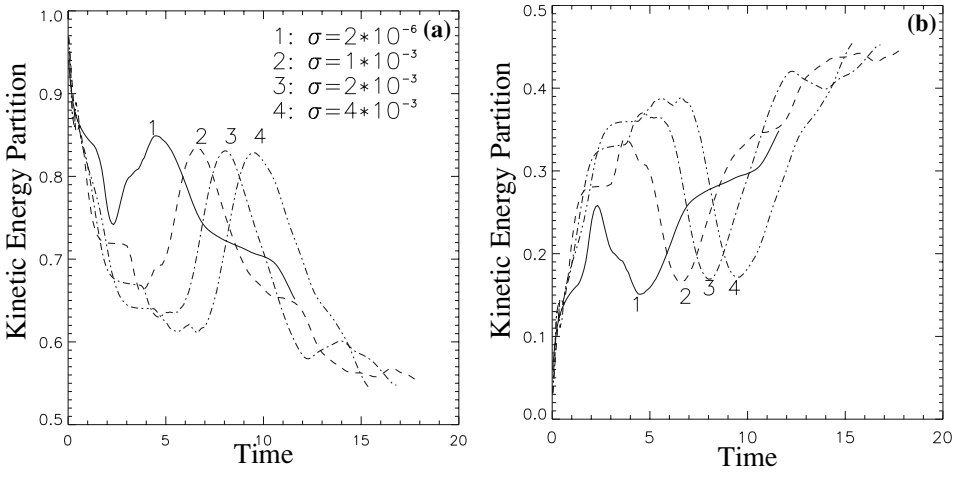

Figure 8. Partition of kinetic energy and its dependence on the surface tension. (a) Vertical (longitudinal) component of the kinetic energy versus time. (b) Total horizontal (transverse) components of the kinetic energy versus time. $\sigma = 2\times10^{-6}$ for the solid line, $\sigma = 10^{-3}$ for the dashed line, $\sigma = 2\times10^{-3}$ for the dash-dotted line and $\sigma = 4\times10^{-3}$ for the dash-dot-dotted line.

where summation over the repeated index l is assumed. For example, the longitudinal partitions in figure 8(a) are $b_{33} + \frac{1}{3}$.

As in the miscible case [11], the longitudinal partition remains above 65% throughout the simulation for $\sigma = 2 \times 10^{-6}$ (solid line in figure 8). It first increases as nonlinearity becomes important shortly after $t \sim t_{\rm nl}$. It soon reaches a maximum before the effective mixing rate reaches its maximum at $t_{\rm max}$ (in table 1). The longitudinal partition then decreases almost uniformly till the end of simulation. With increasing surface tension, the RT mixing flow becomes less anisotropic (broken lines in figure 8). Similar to the small surface tension case, the longitudinal partition reaches a minimum at $t_{\rm nl}$ and reaches a maximum before $t_{\rm max}$. However, with large surface tension the energetic content of the transverse flows is almost half of the total kinetic energy as the instability develops (broken lines in figure 8(b)). This is because the surface tension force acts to minimize the surface area. As a result the longitudinal flow, most effective in stretching the surface in RT mixing, is demoted while the transverse flows are now promoted by the surface tension and contain more kinetic energy. We remark that this redistribution of kinetic energy is similar to situations in MHD turbulence.

The turbulent energy dissipation rate in the RT turbulence is found to be an important quantity in modeling the RT mixing [33]. Defined as

$$\epsilon_{ij} = \nu\left\langle \frac{\partial u_j}{\partial x_k}\frac{\partial u_j}{\partial x_k}\right\rangle, \tag{32}$$

the energy dissipation rate is also a good indicator of anisotropy in turbulence. Figure 9(a) plots the longitudinal partition of the energy dissipation rate, and the corresponding transverse partition (in the x direction) is in figure 9(b). Similar to the kinetic energy partition, surface tension promotes the transverse components. Such a surface tension effect is more pronounced in the energy dissipation rate. For $\sigma = 0.004$, the longitudinal energy dissipation rate is comparable with the transverse counterparts as shown in figure 9. This result implies that modification may be needed in modeling the Rayleigh–Taylor mixing with surface tension.

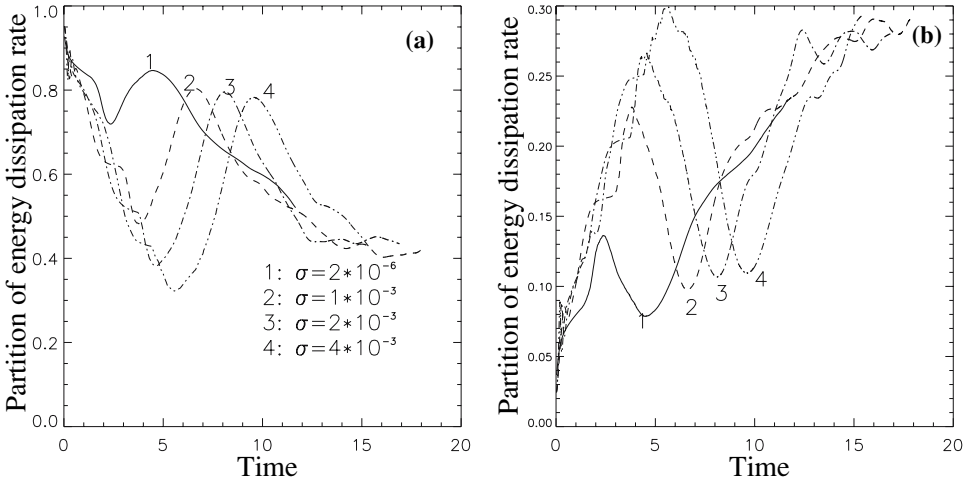

Figure 9. Partition of energy dissipation rate in RT turbulence. (a) The longitudinal partition and (b) the transverse partition in the x direction.

4.2 $\sigma = 0.002$

Here, we focus on how immiscible RT mixing is affected by the density contrast. We present results from simulations with $\sigma = 0.002$ and three different Atwood numbers. The results from these simulations are summarized in table 2. Figure 10(a) shows the bubble height versus time for all three cases. For both $\mathcal{A} = 0.6$ and $\mathcal{A} = 0.3$, nonlinearity takes over at $h_b \sim 0.2$, while for $\mathcal{A} = 0.1$, the nonlinear dominance occurs later at $h_b \sim 0.25$. The maximum effective mixing rate increases with $\mathcal{A}$. The larger the $\mathcal{A}$, the sooner the maximum is reached (figure 10(b)). Interestingly, the mixing zone width at $t_{\max}$ (the time when the effective mixing rate is maximum) is $h \sim 1.9$, insensitive to the Atwood number.

Figure 11 shows the partition of kinetic energy for all three cases. The curves on the top are for the longitudinal partitions, and the bottom three curves are partitions in the x component. In figure 11(a) the partitions are plotted against time, while in figure 11(b) the partitions are plotted against the mixing zone width h. In figure 11 we also find the anisotropy to decrease with the Atwood number. For all three Atwood numbers the longitudinal component starts increasing around $t_{\rm nl}$; it then reaches a maximum before $\alpha_{\rm eff}$ reaches the maximum at $t_{\max}$. For all three Atwood numbers, we find that the anisotropy is amplified right after nonlinearity sets in at $t_{\rm nl}$. There is supporting evidence that the self-similar growth starts at a time between $t_{\rm nl}$ and $t_{\max}$, as will be discussed in section 5. Based on the scaling argument in section 5, the self-similar growth should start around the time when the maximum anisotropy is reached. In addition, the longitudinal partition approaches ~60% at late times (after $t_{\max}$) for $\mathcal{A} = 0.1$ and $\mathcal{A} = 0.3$. The corresponding partitions of energy dissipation rate are shown in figure 12.

Table 2. Summary for $\sigma = 0.002$ simulations. n is the growth rate (dashed lines in figure 5). Again, equation (15) is used to approximate the dominant perturbation wavenumber from the growth rate n.

$\mathcal{A}$	k (2π)	n	k_0	$h_{\rm nl}$	$k_0 \times h_{\rm nl}$	$t_{\rm nl}$	max $(\alpha_{\rm eff})$	$t_{\max}$	h $(t_{\max})$	$\Delta t = t_{\max} - t_{\rm nl}$
0.1	1	0.47	2.35	0.25	0.59	14.3	0.035	23.20	1.88	8.9
0.3	3	1.1	4.4	0.20	0.88	6.0	0.054	10.81	1.90	4.8
0.6	3	1.50	3.91	0.20	0.78	3.8	0.063	7.10	1.89	4.3

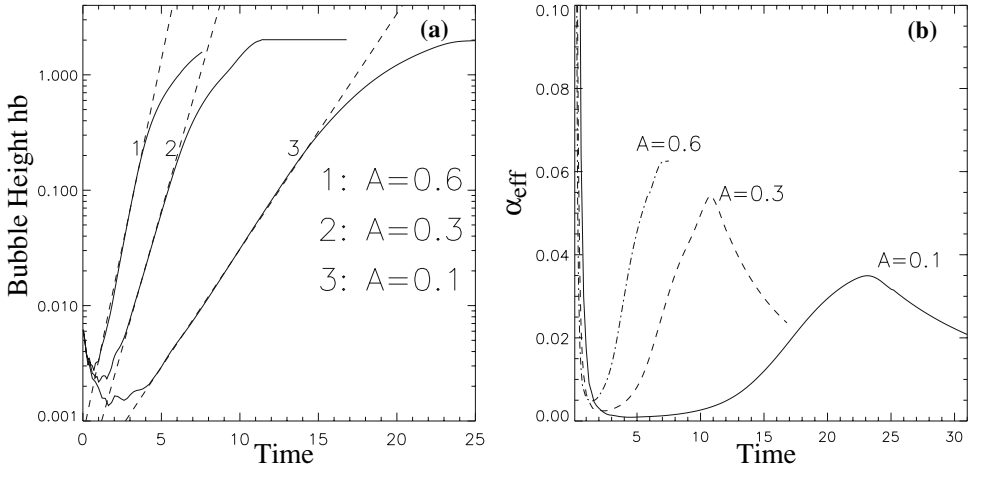

Figure 10. (a) Bubble height versus time for different values of $\mathcal{A}$ on a log-linear plot. $\sigma = 0.002$ for all simulations. (b) The corresponding mixing rate α versus time.

4.3 $\sigma = 4 \times 10^{-6}$

It is well documented that the RT turbulence may depend on the initial conditions [14]. Such dependence may be even more prominent if the Reynolds number is not too high (as in our simulations) [2]. In this subsection, we change the spectrum of the initial random perturbation so that the dominant perturbation wavelengths are smaller than those in sections 4.1 and 4.2. For a smaller dominant perturbation wavelength, the horizontal periodic boundary conditions have less effects on the RT turbulence mixing rate [34]. Thus, the ensuing RT turbulence may be closer to the self-similar turbulence despite the moderate Reynolds number and the finite domain size in our simulations. To investigate how findings in the above sections might be

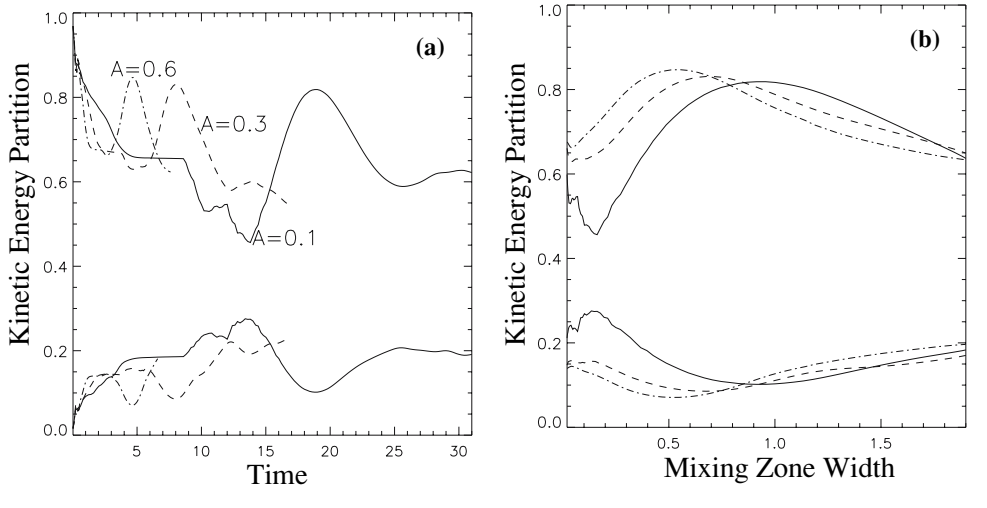

Figure 11. (a) Partition of kinetic energy: the top curves are for longitudinal partition and the bottom curves are partition for one of the transverse components. (b) Partition of kinetic energy with respect to the mixing zone width. The solid lines are for $\mathcal{A} = 0.1$, dashed lines are for $\mathcal{A} = 0.3$ and dash-dotted lines are for $\mathcal{A} = 0.6$.

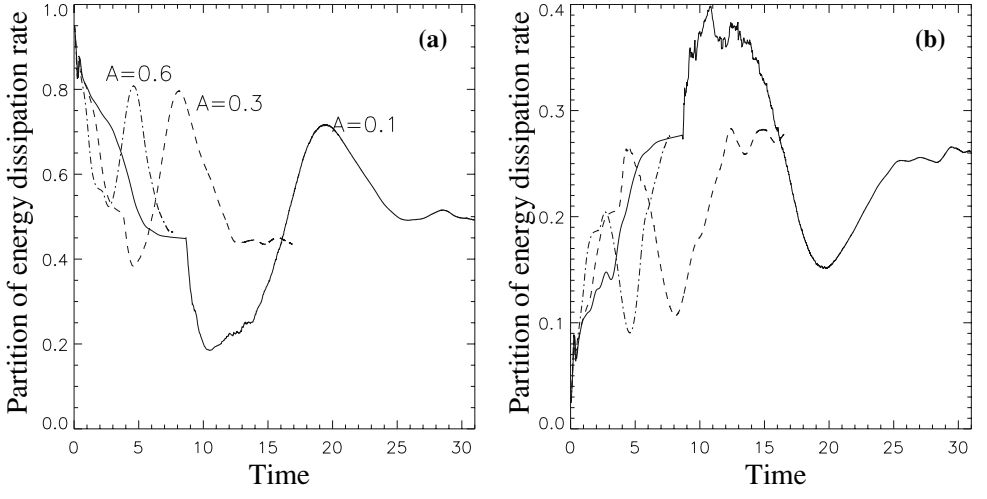

Figure 12. Partition of energy dissipation rate. (a) Longitudinal partition (in the z direction) of the kinetic energy. (b) Transverse partition (in the x direction). The solid lines are for $\mathcal{A} = 0.1$, dashed lines are for $\mathcal{A} = 0.3$ and dash-dotted lines are for $\mathcal{A} = 0.6$.

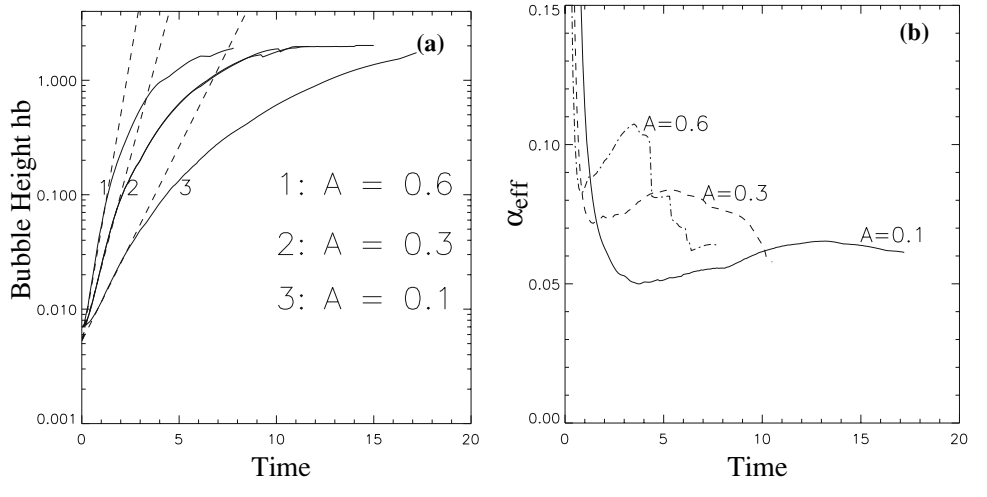

Figure 13. (a) Bubble height versus time for different values of $\mathcal{A}$ on a log-linear plot. $\sigma = 4 \times 10^{-6}$ for all simulations. (b) The corresponding mixing rate α versus time.

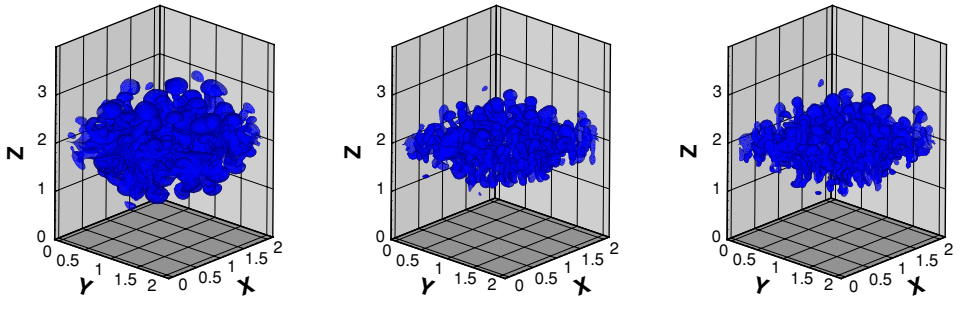

Figure 14. Fluid interface at $t_{\max}$, when the mixing rate reaches a maximum. $\sigma = 4 \times 10^{-6}$. From left to right $\mathcal{A} = 0.1$, $\mathcal{A} = 0.3$ and $\mathcal{A} = 0.6$.

Table 3. Summary for the third set of simulations. n is the growth rate (slope of the dashed lines in figure 13). k_0 is the approximated perturbation wavenumber based on the inviscid dispersion relation (equation (15)) and the computed growth rate n.

σ	$\mathcal{A}$	$k\ (2\pi)$	n	k_0	$h_{\rm nl}$	$k_0 \times h_{\rm nl}$	$t_{\rm nl}$	max $(\alpha_{\rm eff})$	$t_{\rm max}$	$h\ (t_{\rm max})$	$\Delta t = t_{\rm max} - t_{\rm nl}$
4×10^{-6}	0.1	8	0.78	6.13	0.04	0.24	2.70	0.063	13.10	1.08	10.40
4×10^{-6}	0.3	8	1.47	7.74	0.10	0.77	2.11	0.084	5.10	0.73	2.99
4×10^{-6}	0.6	8	2.30	9.25	0.11	1.02	1.40	0.105	3.50	0.77	2.1

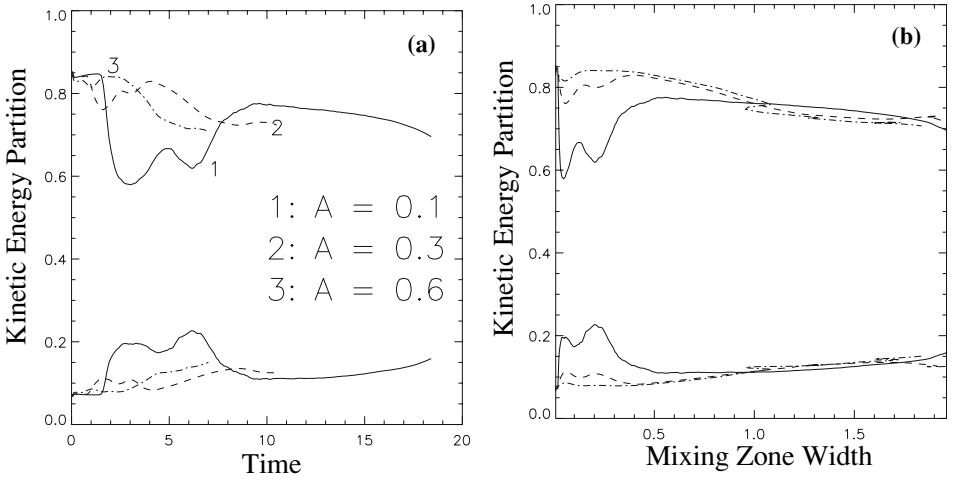

Figure 15. (a) Partition of kinetic energy: the top curves are for longitudinal partition and the bottom curves are partition for one of the transverse components. (b) The same kinetic energy partition versus the mixing zone width. The solid lines are for $\mathcal{A} = 0.1$, dashed lines are for $\mathcal{A} = 0.3$ and dash-dotted lines are for $\mathcal{A} = 0.6$.

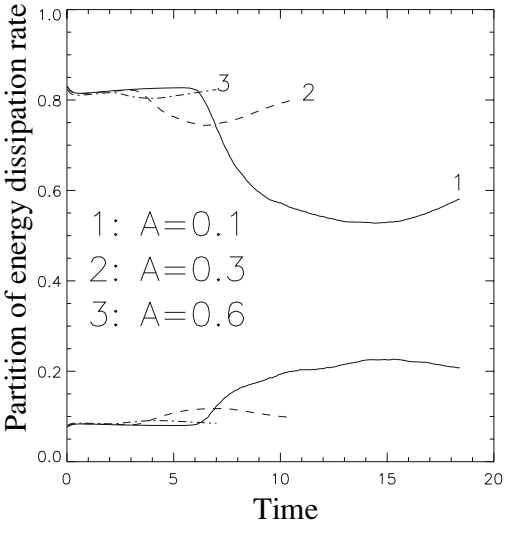

Figure 16. Partition of energy dissipation rate: the top curves are for longitudinal partition and the bottom curves are partition for one of the transverse (x) components. The solid lines are for $\mathcal{A} = 0.1$, dashed lines are for $\mathcal{A} = 0.3$ and dash-dotted lines are for $\mathcal{A} = 0.6$.

altered by a smaller dominant perturbation wavelength λ, we repeat some of the simulations with the surface tension limited to a small value ($\sigma = 4 \times 10^{-6}$) due to the stabilizing effects.

Figure 13 shows the bubble height and the effective mixing rate versus time, and table 3 summarizes the basic characteristics of these simulations. The dominant wavelengths for all these four simulations are around $L/8$. A transition to nonlinear evolution occurs at $h_{\mathrm{nl}} \sim 0.04$ for $\mathcal{A} = 0.1$, while $h_{\mathrm{nl}} \sim 0.1$ for both $\mathcal{A} = 0.3$ and $\mathcal{A} = 0.6$. Compared with the simulations in section 4.2 with longer dominant perturbation wavelengths, we find the effective mixing rate α_{eff} to be larger for smaller dominant wavelengths, and the mixing zone width at $t_{\max}$ slightly depends on the Atwood number. The range of α_{eff} in this set of simulations is similar to that in [7] with similar parameter values and range of perturbation wavelength. For example, the $\mathcal{A} = 0.3$ run in table 3 has parameter values closest to those in [7] with a corresponding surface tension $\sigma' = 6 \times 10^{-4}$. From the FronTier (front-tracking) simulations, the mixing rate $\alpha_b \sim 0.085$ for $\sigma' = 6 \times 10^{-4}$ from figure 2 in [7], consistent with $\alpha_{\mathrm{eff}} = 0.073$ from our simulations. The fluid interface at $t_{\max}$ (when the maximum mixing rate is reached) is illustrated in figure 14 for all three cases.

Figure 15 shows the partition of kinetic energy, similar to the results for larger dominant perturbation wavelengths in section 4.2, the anisotropy in the RT turbulence is decreasing at the end of the simulations. However, we observe stronger anisotropy for cases with smaller dominant perturbation wavelengths. Such stronger anisotropy is also reflected in the energy dissipation rate in figure 16 (cf figure 12).

5. Conclusion

In this paper, we investigate the effect of surface tension on the RT instability and the ensuing mixing. For a single-mode RT instability, we modify the local potential flow analysis in [1] to consider the surface tension effect on the linear stability and the nonlinear terminal bubble velocity. The stabilizing effect of surface tension on the linear growth rate is reproduced (the same as in [21]). The terminal bubble velocity is reduced by surface tension, and these results are in good agreement with numerical simulations of a viscous, single-mode RT instability with $\sigma = 0.002$.

We use the finite-volume, particle-level-set, two-phase flow solver to simulate RT mixing with random perturbations at the interface. The homogeneous Cartesian grid refinement allows us to accurately resolve the flow around the interface with a refined mesh. Such adaptive capability also enables us to capture the interface dynamics efficiently without having to over-resolve the velocity away from the interface. We validate the usage of this code to simulate the immiscible RT instability by comparing with results from the linear and nonlinear analyses. We also show numerical convergence in simulating the RT instability using the FV-PLS flow solver.

We investigate the surface tension effect on the anisotropy in the RT mixing flow. Different values of surface tension and density contrast are used in the simulations. In the RT mixing flow, the surface tension reduces the flow anisotropy, and redistributes some of the kinetic energy from the longitudinal component to the transverse components. For very small surface tension ($\sigma = 2 \times 10^{-6}$), we simulate the "almost miscible" RT mixing with finite density contrast $\mathcal{A} = 0.3$. Results from this simulation are consistent with those from Boussinesq miscible RT simulations [13]; nonlinearity sets in at t_{nl} before the initiation of self-similar growth, which is around $15t_c = 3.35$. As the self-similar process begins, the effective mixing rate α_{eff} first increases, reaches a maximum at $t_{\max}$ and then settles to an asymptotic constant if the conditions are sufficient for turbulence to develop.

For the Boussinesq miscible RT instability [13], the turbulence is estimated to become fully developed in the RT mixing zone at around $t \sim 40t_c$ after the onset of the self-similar growth at $t_s = 15t_c$. Large density contrast ($\mathcal{A} = 0.3$) gives rise to larger effective acceleration $\alpha \mathcal{A} g$; thus, the mixing zone may reach the wall before the flow can evolve into turbulence. Consequently for sufficiently large Reynolds number and numerical resolution, the minimum computation domain for the RT mixing flow to develop into turbulence increases with the Atwood number. In the "almost" miscible case (with $\mathcal{A} = 0.3$ and $\sigma = 2 \times 10^{-6}$), the simulation continues till $t \sim 50t_c = 11.16$ and the mixing zone has already reached the wall. Thus, the RT mixing flow has not yet become fully turbulent in our simulations (including those with higher surface tension). Indeed, at the end of the simulations, the Weber number (defined as $We \equiv 4(\rho_1 + \rho_2)h^3/t^2\sigma$ [35]) is in the range of $We \sim 800$, considerably lower than the range quoted in Dimonte and Schneider's experiments [35]. In addition, the Reynolds number in our simulations is in the range of $Re \sim 2h^2/(t\nu) \sim 10^3$, also lower than that in the experiments. Thus the RT turbulence in our simulations is not yet well into the self-similar regime, and consequently the dependence of α on the bubble aspect ratio D/h (D is the bubble diameter) may not be as prominent as its dependence on the Froude number. As a result, α decreases with increasing surface tension in our simulations as opposed to the increasing trend by the surface tension reported in experiments [35], where a surfactant has been used to control the strength of the surface tension.

On the other hand, recent results from front-tracking direct numerical simulation of inviscid, immiscible RT chaotic mixing report that the mixing rate α decreases with increasing σ [7]. In these simulations, the Weber number and Reynolds number are quite close to the range in the experiments: $We \sim 3761$ and $Re \sim 10^5$ (based on the numerical viscous dissipation in their front-tracking simulations [36]). Thus, it is possible that the trend of increasing α with increasing surface tension in experiments may be partly due to the surfactant, which not only reduces surface tension but also induces Marangoni stresses that alter the flow around the fluid interface. The presence of a surfactant also causes large deformation of fluid interface and retards pinch-off [37], which is consistent with the larger aspect ratio (self-similarity parameter) D/h found in the experiments with surfactants. We will start an investigation on the surfactant effects on the RT chaotic mixing and turbulence. We plan to focus on how the surfactant may lead to increasing α. In particular, we will explore first the effects of an insoluble surfactant, and will include surfactant solubility in the future.

From the $\mathcal{A} = 0.3$ simulations we observe that, right after the nonlinearity takes over the initial linear growth, anisotropy begins to amplify until the onset of the self-similar growth. This is illustrated in figure 17, where we plot the ratio of transverse partition to longitudinal partition of the kinetic energy. A small ratio means strong anisotropy in the flow, and tick marks on the figure indicate t_{nl} for different values of σ. Focusing on the solid line in figure 17 ($\sigma = 2 \times 10^{-6}$ in this case), we find that the ratio starts to increase at $t \sim 4$, which is close to the time $t_s = 15t_c$ when the self-similar growth initiates for the miscible case ($\sigma = 0$). The increase in the partition ratio is an indication of the self-similar growth because anisotropy decreases as turbulence develops and energy cascades from large to small scales. Thus, the reduction in the partition ratio at $t \sim t_{\mathrm{nl}}$ can be viewed as a pre-requisite condition for the self-similar growth. To elucidate this argument, we adopt the self-similar analysis for the Boussinesq RT turbulence [13] with a key modification in the balancing of terms.

In the self-similar analysis, the existence and validity of the self-similar solution hinges on a particular balance of terms in moment equations obtained from averaging the Navier–Stokes momentum equations. The averaging procedure, indicated by the angle brackets, is the standard planar average $\langle f \rangle = (1/L^2) \int f \mathrm{d}x\mathrm{d}y$. Here we seek a suitable scaling that corresponds to the arisotropic conditions (prior to fully developed turbulence) that still allow for the (onset

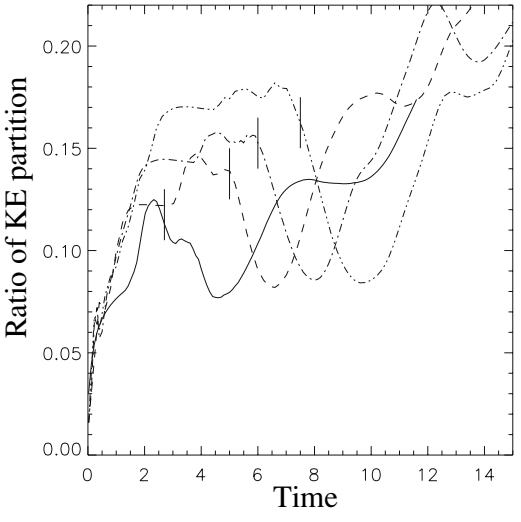

Figure 17. Ratio of kinetic energy partition: x component to z component for $\mathcal{A} = 0.3$ simulations. Solid line: $\sigma = 2 \times 10^{-6}$, dashed line: $\sigma = 0.001$, dash-dotted line: $\sigma = 0.002$ and dash-dot-dotted line: $\sigma = 0.004$. The tick marks indicate the onset of nonlinearity t_{nl} from table 1.

of the) self-similar solution. To this end, we find the following scaling:

$$\partial_t \to \epsilon \partial_{t'}, \quad \partial_x \to \epsilon^m \partial_{x'}, \quad \partial_y \to \epsilon^m \partial_{y'}, \quad \partial_z \to \epsilon^2 \partial_{z'},$$
$$p \to \frac{p'}{\epsilon^2}, \quad u \to \frac{u'}{\epsilon^{m-1}}, \quad v \to \frac{v'}{\epsilon^{m-1}}, \quad w \to \frac{w'}{\epsilon}, \tag{33}$$

with $\epsilon \ll 1$ and $m > 1/2$. Applying the above scaling with $m = 1$ to the first-order and second-order moment equations in [13], we obtain (dropping the primes)

$$\langle w^2 \rangle_z = -P_z - \mathcal{A}gC, \quad \partial_t C + \langle wc \rangle_z = 0, \tag{34}$$
$$\partial_t \langle wc \rangle + \langle w^2 c \rangle_z = -\langle w^2 \rangle C_z - \mathcal{A}g \langle c^2 \rangle - \langle cp_z \rangle, \tag{35}$$
$$\partial_t \langle c^2 \rangle + \langle wc^2 \rangle_z = -2\langle wc \rangle C_z, \tag{36}$$
$$\partial_t \langle w^2 \rangle + \langle w^3 \rangle_z = -2\mathcal{A}g \langle wc \rangle - 2\langle wp \rangle_z, \tag{37}$$
$$-\mathcal{A}g \langle wc \rangle = \langle wp \rangle_z, \tag{38}$$

where P (mean pressure) and C (mean density) are the only non-zero first-order moments, and w and c are fluctuations in the longitudinal velocity and density, respectively. Due to the scaling (equation (33)) the molecular dissipative and diffusive terms in the original moment equations (equations (2.7)–(2.10) and (2.12) in [13]) drop out at leading order in ϵ. Applying the self-similar analysis in [13] to equations (34)–(38), we obtain the following self-similar solution:

$$h(t; C_0, t_0) = \frac{1}{4} \mathcal{A}gC_0 t_0^2 (\tau + 1)^2, \quad t_0 = \sqrt{\frac{4h_0}{\mathcal{A}gC_0}} \tag{39}$$

and other self-similar temporal behaviors that are found in [13]. Based on the above results, we conclude that the scaling in equation (33) implicates the strong anisotropy necessary for "cultivating" the onset of the self-similar turbulence. However, based on the turbulence theory, once the self-similar mixing starts the large-scale anisotropy will be reduced to small-scale

anisotropy or completely diminished for high enough Reynolds numbers. Thus, we can reasonably expect equation (33) to be a prelude to the self-similar growth in equation (39) and we would not expect equation (33) to hold as turbulence develops. As a result, the scaling behavior (such as $w : u \to 1 : \epsilon$) is an indicator for the onset of the self-similar RT turbulence.

We remark that the quadratic growth of the mixing zone $h = \alpha \mathcal{A} g t^2$ may continue as long as there exists local velocity anisotropy (described by equation (33)) near the edge of the mixing zone. In our future work, we will verify this and find a more rigorous condition for the detection of the self-similar turbulence growth in the RT turbulence. Abarzhi *et al*. suggested specific scaling behavior for the self-similar turbulence; the vertical energy dissipation rate scales linearly with time, and the rate of momentum loss remains constant [33]. We will investigate these scaling behaviors in our numerical simulations of the RT turbulence, and investigate which one is the best indicator for the onset of the self-similar RT turbulence.

Acknowledgements

We acknowledge the support from the NSF/MRI funded computing cluster at NJIT/DMS. We wish to thank J. Glimm, X. Li, Y. Zhang, P. Ramaprabhu and M. Siegel for helpful discussion.

References

[1] Goncharov, V.N., 2002, *Physical Review Letters*, **88**, 134502.
[2] Cook, A.W. and Dimotakis, P.E., 2001, *Journal of Fluid Mechanics*, **443**, 69.
[3] Ramaprabhu, P. and Andrews, M.J., 2004, *Physics of Fluids*, **16**, L59.
[4] Ramaprabhu, P., Dimonte, G. and Andrews, M.J., 2005, *Journal of Fluid Mechanics*, **536**, 285.
[5] Glimm, J., Grove, J.W., Li, X., Oh, W. and Sharp, D.H., 2001, *Journal of Computational Physics*, **169**, 652.
[6] Dimonte, G., Youngs, D.L., Dimits, A., Weber, S., Marinak, M., Wunsch, S., Garasi, C., Robinson, A., Andrews, M.J., Ramaprabhu, P., et al., 2004, *Physics of Fluids*, **16**, 1668.
[7] George, E., Glimm, J., Li, X., Li, Y. and Liu, X., 2006, *Physical Review E*, **73**, 016304.
[8] Jin, H., Liu, X.F., Lu, T., Cheng, B., Glimm, J. and Sharp, D.H., 2005, *Physics of Fluids*, **17**, 1.
[9] Linden, P.F., Redondo, J.M. and Youngs, D.L., 1994, *Journal of Fluid Mechanics*, **265**, 97.
[10] Dalziel, S.B., Linden, P.F. and Youngs, D.L., 1999, *Journal of Fluid Mechanics*, **399**, 1.
[11] Young, Y.-N., Tufo, H., Dubey, A. and Rosner, R., 2001, *Journal of Fluid Mechanics*, **447**, 377.
[12] Ramaprabhu, P. and Andrews, M.J., 2004, *Journal of Fluid Mechanics*, **502**, 233.
[13] Ristorcelli, J.R. and Clark, T.T., 2004, *Journal of Fluid Mechanics*, **507**, 213.
[14] Dimonte, G., 2004, *Physical Review E*, **69**, 056305.
[15] Chertkov, M., 2003, *Physical Review Letters*, **91**, 115001.
[16] Fermi, E., 1951, *The Collected Papers of Enrico Fermi*, In E. Segre (Ed.) vol. 2, pp. 816–821 (Chicago: University of Chicago Press).
[17] Layzer, D., 1955, *Astrophysical Journal*, **122**, 1.
[18] Hecht, J., Alon, U. and Shvarts, D., 1994, *Physics of Fluids*, **6**, 4019.
[19] Ramaprabhu, P. and Dimonte, G., 2005, *Physical Review E*, **71**, 0363141.
[20] Sohn, S.-I., 2004, *Physical Review E*, **69**, 036703.
[21] Chandrasekhar, S., 1961, *Hydrodynamic and Hydromagnetic Instability* (New York: Dover).
[22] Ham, F.E., Lien, F.S. and Strong, A.B., 2002, *Journal of Computational Physics*, **179**, 469.
[23] Jiang, G.-S. and Peng, D., 2000, SIAM *Journal of Scientific Computing*, **21**, 2126.
[24] Enright, D., Fedkiw, R., Ferziger, J. and Mitchell, I., 2002, *Journal of Computational Physics*, **183**, 83.
[25] Young, Y.-N., Ferziger, J., Ham, F. and Herrmann, M., 2003, Center for Turbulence Research Annual Research Briefs, http://ctr.stanford.edu/ResBriefs03/yyoung1.pdf
[26] Sussman, M., Smereka, P. and Osher, S., 1994, *Journal of Computational Physics*, **114**, 146.
[27] Tornberg, A.-K., 2005, in Laptev, A. (ed.), European Congress of Mathematics (ECM), Stockholm, Sweden, June 27–July 2, 2004. (Zurich: European Mathematical Society), pp. 477–429.
[28] Kim, D. and Choi, H., 2000. *Journal of Computational Physics*, **162**, 411.
[29] Tryggvason, G., Bunner, B., Esmaeeli, A., Juric, D., Al-Rawahi, N., Tauber, W., Han, J., Nas, S. and Jan, Y.-J., 2001, *Journal of Computational Physics*, **169**, 708.
[30] Clavin, P. and Williams, F., 2005, *Journal of Fluid Mechanics*, **525**, 105.
[31] Glimm, J., Li, X.-L. and Lin, A.-D., 2002, Acta Mathematicae Applicatea Sinica, **18**, 1.
[32] Ramaprabhu, P., Dimonte, G., Young, Y.-N., Fryxell, B. and Calder, A.C., 2005, in preparation.
[33] Abarzhi, S.I., Gorobets, A. and Sreenivasan, K.R., 2005, *Physics of Fluids*, **17**, 081705.

[34] Glimm, J., Grove, J.W., Li, X.L., Oh, W. and Sharp, D.H., 2001, *Journal of Computational Physics*, **169**, 652.
[35] Dimonte, G. and Schneider, M., 2000, *Physics of Fluids*, **12**, 304.
[36] Liu, X., 2006, private communication.
[37] Stone, H.A., 1994, *Annual Review of Fluid Mechanics*, **26**, 65.
[38] Chertkov, M., Kolokolov, I. and Lebedev, V., 2005, *Physical Review* E, **71**, 055301.
[39] Cook, A.W. and Zhou, Y., 2002, *Physical Review E*, **66**, 026312.